Materials Advances

PAPER

View Article Online
View Journal | View Issue

Cite this: *Mater. Adv.*, 2021, 2, 5479

Design of ternary Pt–CoZn alloy catalysts coated with N-doped carbon towards acidic oxygen reduction†

Xieweiyi Ye, Yakun Xue, Kaijia Li, Wen Tang, Xiao Han, Xibo Zhang, Zhijia Song, Zhiping Zheng and Qin Kuang *

Improving the activity and durability of Pt-based electrocatalysts used in the acidic oxygen reduction reaction (ORR) is a great task for the commercial application of proton-exchange membrane fuel cells. Alloying with transition metal elements is one of the most promising strategies, but it is still accompanied by poor catalyst durability due to the leaching of transition metal components. Herein, we report a facile pyrolysis approach for fabricating N-doped carbon-coated Pt-based ternary alloy nanoparticles (Pt–CoZn@NC) by using Co/Zn-based bimetallic zeolitic imidazolate framework-encapsulated Pt nanoparticles (Pt@CoZn-ZIF) as precursors. After optimizing the experimental conditions, the Pt–CoZn@NC-800-10% catalyst exhibited outstanding activity ($E_{1/2}$: 0.917 V *vs.* RHE) and stability ($E_{1/2}$ after 5000 cycles: 1 mV), which are superior to those of binary Pt-based alloy catalysts (*i.e.*, Pt–Co@NC and Pt–Zn@NC) and commercial Pt/C catalysts in the acidic ORR. Such enhanced performances are attributed to the favourable ternary alloy structure, which promoted electronic interactions among metal species (Pt, Co, and Zn). A ZIF-derived NC matrix helps to improve the conductivity and catalytic durability due to an increased number of active sites. This work provides a feasible strategy for preparing efficient and stable Pt-based ternary alloy ORR electrocatalysts.

Received 29th May 2021,
Accepted 11th July 2021

DOI: 10.1039/d1ma00475a

rsc.li/materials-advances

Introduction

Acidic oxygen reduction reaction (ORR) catalysts with high activity and excellent durability are crucial for developing high-performance proton-exchange membrane fuel cells (PEMFCs).[1] Over the past few decades, conventional carbon-supported Pt catalysts have been extensively applied to overcome the sluggish ORR kinetics at fuel cell cathodes;[2,3] however, the scarcity, increased cost, and poor durability of Pt greatly limit its large-scale practical applications.[4–7] Alloying Pt with transition metals M (M = Fe, Co, Ni, Cu, Zn, *etc.*)[8–12] is a promising strategy for reducing the consumption of Pt and also promoting the ORR catalytic performance by fine-tuning the electronic structure *via* ligand or surface strain effects.[13,14] Among such alloys, Pt–Co exhibits outstanding ORR activity,[15–18] but it still suffers from transition metal leaching from alloys during electrocatalytic processes.[19,20] Therefore, methods to improve the performance of Pt–Co catalysts are of great practical importance.

To improve the overall electrocatalytic performance, an attractive method is to construct Pt–Co-based ternary alloy systems with a multi-metallic synergistic effect, such as PtCoW,[20] PtCoNi,[21] PtFeCo/NPG,[22] PtCoMn,[23] *etc.* The introduction of a third metal provides flexibility for manipulating the electronic and/or surface structure, which can greatly alter the availability of surface active sites and remarkably enhance the ORR performance.[14,24] In addition, embedding Pt-based alloy catalysts onto N-doped carbon (NC) is an effective strategy because the NC matrix can increase the electron density at active sites and inhibit the dissolution or leaching of transition metal atoms due to its high electronic conductivity and high affinity for metal NPs.[25–31] Clearly, if the above two strategies can be integrated using a simple method, the activity and durability of Pt-based alloy catalysts will be greatly improved.

In this study, we report a facile pyrolysis route to fabricate NC-coated Pt-based ternary alloy (Pt–CoZn@NC) catalysts with a plum-pudding architecture. Zn/Co bimetallic zeolitic imidazolate frameworks (ZIFs, a subclass of metal–organic frameworks comprised of imidazolate linkers and metal ions[30]) encapsulated with Pt nanoparticles (NPs) were selected as the precursors of the hybrid catalysts.[31,32] In the architecture of Pt–CoZn@NC, Zn was doped into the Pt–Co alloy and readily donated its valence electrons to other components due to its lower electronegativity, thereby forming a more optimized

---

Department of Chemistry, College of Chemistry and Chemical Engineering, Xiamen University, Xiamen 361005, Fujian, P. R. China.
E-mail: qkuang@xmu.edu.cn; Fax: +86-592-2183047

† Electronic supplementary information (ESI) available. See DOI: 10.1039/d1ma00475a

electronic structure in Pt–CoZn alloy catalysts.[33] Furthermore, the ZIF-derived NC matrix played an important role in modifying the electronic structure of the Pt-based alloy and positively influencing electron transfer and electrocatalytic activity owing to the high-proportion pyridinic N and graphite N species.[34,35] As expected, this ternary Pt–CoZn@NC hybrid nanostructure exhibited significantly enhanced electrocatalytic performance in the acidic ORR, outperforming commercial Pt/C and binary alloy-based catalysts (Pt–Zn@NC and Pt–Co@NC).

Experimental section

Materials and chemicals

Chloroplatinic acid ($H_2PtCl_6{\cdot}6H_2O$), zinc nitrate hexahydrate ($Zn(NO_3)_2{\cdot}6H_2O$), cobalt(II) nitrate hexahydrate ($Co(NO_3)_2{\cdot}6H_2O$), polyvinylpyrrolidone (PVP, K-30), acetone, methanol, and ethanol were purchased from Sinopharm Chemical Reagent Co. Ltd (Shanghai, China). 2-Methylimidazole was purchased from J.K. All reagents were used as received without further purification. Ultrapure water was used throughout all experiments.

Synthesis of Pt@MOF precursors

First, polyvinylpyrrolidone (PVP, K-30) capped Pt NPs were prepared according to previously reported methods.[36,37] They were then dispersed in methanol to obtain a solution with a concentration of 5 mg mL^{-1}. Next, 80 mL of 2-methylimidazole methanol solution (1.68 mol L^{-1}) and 7.43 mL of prepared PVP-capped Pt NP solution were uniformly mixed by magnetic stirring. The bimetallic ZIF containing Zn and Co in different molar ratios (total metal ion molarity = 3.12 mmol) was mixed into 6 mL of methanol solution along with ultrasonic dispersion. Then, it was slowly added into the above solution accompanied by vigorous stirring for 6 h at room temperature. The precipitate was centrifuged and washed with ethanol several times, followed by drying at 60 °C under vacuum overnight. For comparison, Pt@ZIF-8 and Pt@ZIF-67 were synthesized following the same procedures using PVP-capped Pt NPs stock solution and $Zn(NO_3)_2{\cdot}6H_2O$ or $Co(NO_3)_2{\cdot}6H_2O$, respectively. The theoretical Pt loading was about 5 wt% according to the ratio of Pt NPs relative to ZIFs. The Pt@MOF precursors with different Pt loading were denoted as Pt@ZIF-8-*W*, Pt@ZIF-67-*W*, and Pt@CoZn-ZIF-*W* (*W* = 1%, 5%, 10%).

Synthesis of Pt–Zn@NC, Pt–Co@NC, and Pt–CoZn@NC hybrid catalysts

The Pt@MOF samples were first transferred to a quartz boat in a tube furnace. Then, the Pt@MOF samples were heated at 200 °C for 1 h to remove guest molecules in the MOF cavities and then heated to a higher temperature (700, 800, 900 °C) for 5 h with a heating rate of 5 °C min^{-1} in a H_2/Ar flow (5 : 95 volume ratio). For convenience, the resulting products were denoted as Pt–Zn@NC-*X*-W, Pt–Co@NC-*X*-*W* and Pt–CoZn@NC-*X*-*W* (*X* = 700, 800, 900; *W* = 1%, 5%, 10%) according to the pyrolysis temperature and Pt loading.

Characterization of samples

A transmission electron microscope (TEM, JEOL2100) operated at 200 kV and a scanning electron microscope (SEM, Hitachi S4800) equipped with energy-dispersive X-ray spectroscopy (EDS) were used to identify the morphology and elemental composition of the samples. High-angle annular dark-field scanning transmission electron microscopy (HAADF-STEM) images and EDS line scan/mapping profiles were obtained with a FEI TECNAI F30 microscope operated at 300 kV. Powder X-ray diffraction (XRD) patterns were tested by a Rigaku Ultima IV diffractometer using Cu-Kα radiation (40 kV, 30 mA). Thermogravimetric analysis and differential scanning calorimetry (Simultaneous TGA-DSC) were performed on an SDT Q600 simultaneous thermal analyzer. Three precursors were heated from 100 to 800 °C (10 °C min^{-1}) in a N_2 flow. X-Ray photoelectron spectroscopy (XPS) measurements were performed on a PHI Quantum 2000 Scanning ESCA Microprobe using monochromatic Al-Kα X-rays as the excitation source. Here, the charged displacement of samples was corrected using the C 1s line (284.8 eV). Raman spectra (XploRA INV HORIBA) were recorded at room temperature using a 532 nm laser beam with powder samples on glass slides. Inductively coupled plasma mass spectrometry (ICP-MS, Agilent 7700×) was used to measure the Co, Zn, and Pt content in each sample.

Electrochemical measurements

Electrochemical measurements were carried out using an electrochemical workstation (CHI 760E, Shanghai Chen Hua Co., China) with a three-electrode system at room temperature (25 °C). A glassy carbon (GC) rotating disk electrode (RDE, Pine Research Instrumentation) with a diameter of 5 mm served as the working electrode. A platinum net and a saturated calomel electrode (SCE) were chosen as the counter and reference electrodes, respectively. Well-dispersed catalysts were prepared by dissolving catalysts in a mixture of ethanol, water, and Nafion (400 : 400 : 1) by sonication. The total Pt loading on the working electrode for each measurement was 4 μg according to ICP-MS measurements. All of the given potentials were converted into the reversible hydrogen electrode (RHE) potential. The cyclic voltammetry (CV) curves were recorded over the potential range of 0.05 to 1.05 V *vs.* RHE in N_2-saturated 0.1 M $HClO_4$ solution at a sweep rate of 100 mV s^{-1}. After stable CVs were obtained, the electrocatalytic activity of the ORR was measured by linear sweep voltammetry (LSV) over the potential range of 0.05 to 1.05 V *vs.* RHE at a sweep rate of 10 mV s^{-1} in O_2-saturated 0.1 M $HClO_4$ solution at 25 °C. The accelerated durability tests (ADTs) were performed by potential cycling at 0.6 to 1.0 V (100 mV s^{-1}) in O_2-saturated 0.1 M $HClO_4$ solution. All the RDE tests were measured at a rotation rate of 1600 rpm, and all polarization curves were 85% iR corrected. The current was normalized in terms of the electrode area (0.196 cm^2). The electrochemical active surface area (ECSA) was determined from the hydrogen adsorption area subtracted by the double-layer in the CV curve with a Pt capacity of 210 μC cm_{Pt}^{-2}.

Results and discussion

Catalyst characterizations

Fig. 1 illustrates the synthetic process of Pt-CoZn@NC catalysts. Briefly, PVP-capped Pt NPs (5.1 ± 0.5 nm, Fig. S1, ESI†) were first encapsulated within the Co/Zn bimetallic ZIF, and then the resulting Pt@CoZn-ZIF precursors were calcined under a H_2/Ar atmosphere. For comparison, two binary alloy-based control catalysts, *i.e.*, Pt-Zn@NC and Pt-Co@NC, were synthesized *via* similar synthetic routes using Pt@ZIF-8 and Pt@ZIF-67 precursors, respectively. All precursors exhibited a well-defined rhombic dodecahedral morphology and the same crystallographic structure (Fig. S2, ESI†). Of note, the color and thermogravimetric properties of Pt@CoZn-ZIF were between those of Pt@ZIF-8 and Pt@ZIF-67, suggesting the existence of Co and Zn in the MOF matrix of Pt@CoZn-ZIF.

To reveal the structure of these samples, detailed TEM analysis was conducted. As shown in Fig. 2a, Pt NPs were encapsulated within the CoZn-ZIF matrix without aggregation. Taking the sample with 10 wt_{Pt}% calcined at 800 °C (*i.e.*, Pt–CoZn@NC-800-10%) as a representative, we found that metallic NPs with sizes of 4–20 nm were embedded within the carbon matrix (Fig. 2b). HRTEM images revealed that the carbon shell coated on the surface of metal NPs was very thin (Fig. S3, ESI†), and the lattice fringe spacing of 0.34 nm corresponding to the (002) plane of graphitized carbon can be faintly observed, as shown in Fig. 2c.[36,38] The interplanar spacing of the (111) lattice fringes recorded in metal NPs was measured to be 0.21 nm, which falls between that of Pt (0.226 nm, PDF#04-0802) and Co (0.205 nm, PDF#15-0806). This phenomenon was attributed to the alloying of Pt, Co, and Zn, which is also visualized in both the line scanning profile (Fig. 2d) of an individual metal NP and the element maps (Fig. 2e and f) of the whole Pt-CoZn@NC-800-10% structure. According to the ICP-MS result (Table S1, ESI†), the mass ratios of Pt, Co, and Zn in Pt–CoZn@NC-800-10% are 18.3 wt%, 31.9 wt%, and 9.3 wt%, respectively. In addition, the N and C signals (Fig. 2f) coexisted in the Pt–CoZn@NC-800-10% nanostructure, indicating that nitrogen atoms from 2-methylimidazole were uniformly doped into the carbon matrix. All of the above results demonstrate the ternary alloy nature of metal NPs embedded in the N-doped carbon matrix.

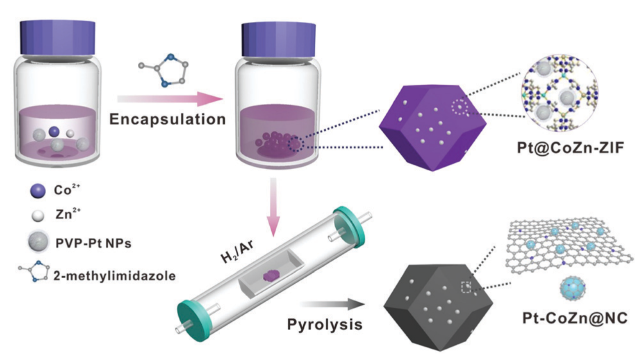

Fig. 1 Synthetic strategy of Pt–CoZn@NC catalysts derived from a Pt@CoZn-ZIF precursor *via* pyrolysis.

The alloying features of Pt-based NPs can also be observed in the Pt–Co and Pt–Zn binary-alloy hybrid structures obtained from the pyrolysis of Pt@ZIF-8 and Pt@ZIF-67 precursors, respectively (Fig. S4, ESI†). It should be noted that the Pt-based alloy NPs in the Pt–Zn@NC-800-10% are highly uniform in size, while those in the two Co-containing samples (*i.e.*, Pt–CoZn@NC-800-10% and Pt–Co@NC-800-10%) tend to aggregate, causing a broad size distribution (Fig. S5, ESI†). In particular, several large alloy particles (approximately 30 nm) with severe agglomeration were observed in Pt–Co@NC-800-10%. This phenomenon was closely related to the ferromagnetism of the Co atoms. However, the Zn species spatially isolated the Co species, which promoted the pyrolysis of the bimetallic ZIF matrix and restricted the agglomeration of Pt–Co alloy NPs.[39,40]

Fig. 2g shows the XRD patterns of three samples. All diffraction peaks of Pt–CoZn@NC-800-10% and Pt–Co@NC-800-10% were indexed as a face-centered cubic (fcc) solid solution alloy. Of note, each diffraction peak of Pt–CoZn@NC-800-10% shifted to lower angles compared with Pt–Co@NC-800-10%, which was caused by the larger atomic radius of Zn than Co. Different from the two Co-containing samples, the XRD pattern of Pt-Zn@NC-800-10% was well-indexed to the tetragonal phase of the intermetallic PtZn alloy (PtZn-PDF#06-0604).[41]

The surface composition and oxidation state of the catalysts were investigated by XPS. The N 1s spectra (Fig. 3a) can be fitted to four main peaks: pyridinic N (398.3 ± 0.1 eV), pyrrolic N (399.6 ± 0.2 eV), graphitic N (401.1 ± 0.2 eV), and oxidized N (404.3 ± 0.2 eV). The pyridinic N and graphitic N, which helped to accelerate electron transfer and increased the diffusion limiting current, notably enhancing the catalytic activity of the ORR.[41,42] The total amount of those two nitrogen species in Pt–CoZn@NC-800-10% accounted for 65.4%, which is higher than that of Pt–Co@NC-800-10% (61.6%) and Pt–Zn@NC-800-10% (62.9%). The Pt 4f XPS spectra (Fig. 3b) show that the binding energies of the Pt 4f peaks assigned to metallic states in the Pt–Co@NC-800-10% (75.02 eV for Pt $4f_{5/2}$; 71.67 eV for Pt $4f_{7/2}$) shifted towards higher binding energies compared with Pt–Zn@NC-800-10% (74.64 eV for Pt $4f_{5/2}$; 71.29 eV for Pt $4f_{7/2}$). The peaks of Pt–CoZn@NC-800-10% (74.85 eV for Pt $4f_{5/2}$; 71.50 eV for Pt $4f_{7/2}$) lay somewhere in between these two. The shift of the Pt peaks was closely related to the electron transfer between Pt and the other two transition metals (Co and Zn). Among the three metal atoms, the electronegativity of Pt is the highest, while Zn is the lowest (Pt: 2.28, Co: 1.88, Zn: 1.65).[43] When Pt was alloyed with Co or Zn, electron transfer from Co or Zn to Pt occurred, thus altering the electron density around the Pt atoms. The XPS spectra of Co 2p (Fig. 3c) and Zn 2p (Fig. 3d) illustrate the coexistence of metallic and oxidized states. As for the ternary Pt–CoZn@NC-800-10%, both Co and Zn helped modify the electronic structure of Pt in terms of the ligand effect and synergistic effect,; thus decreasing the d-band center of Pt species and improving the electrocatalytic performance.[44,45]

Electrocatalytic performance

The ORR catalytic performances of NC-coated Pt-based alloy catalysts were evaluated by RDE. The CV curves (Fig. S6, ESI†)

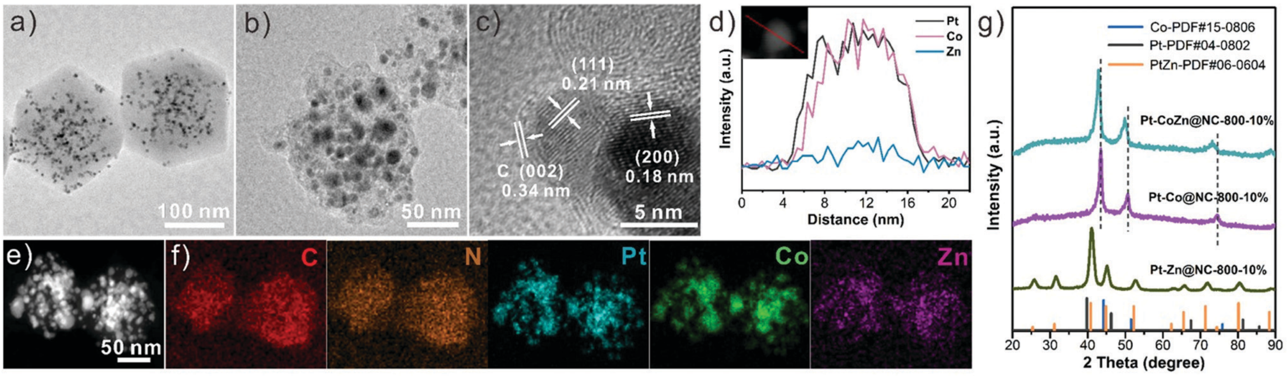

Fig. 2 TEM images of (a) Pt@CoZn-ZIF-10% precursor and (b) Pt–CoZn@NC-800-10% catalyst. (c) HRTEM image of alloy NPs embedded in the carbon matrix of Pt–CoZn@NC-800-10%. (d) EDS line-scan profile and (e and f) HAADF-STEM image with corresponding element maps of the Pt–CoZn@NC-800-10% catalyst. (g) XRD patterns of the pyrolysis products obtained using different precursors.

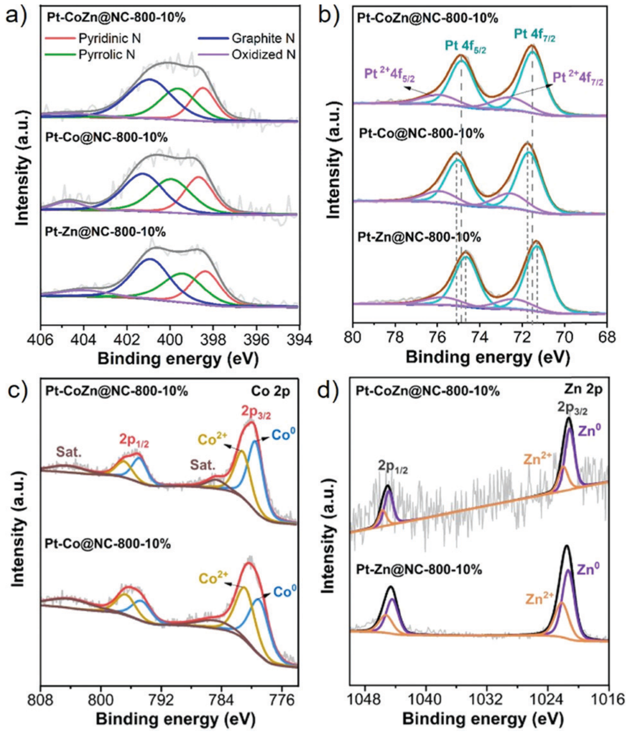

Fig. 3 XPS spectra of (a) N 1s, (b) Pt 4f, (c) Co 2p, and (d) Zn 2p of the three products.

showed the intrinsic property of Pt-based catalysts in terms of both the hydrogen underpotential (H_{upd}) desorption/adsorption peak and the oxide formation/reduction peak.[46,47] Polarization curves of the catalysts were recorded in O_2-saturated 0.1 M $HClO_4$ with a sweep rate of 10 mV s^{-1} at room temperature. As shown in Fig. 4a, the Pt–CoZn@NC-800-10% catalyst exhibited superior electrocatalytic activity with the highest onset potential (E_{onset} = 1.012 V *vs.* RHE) and half-wave potential ($E_{1/2}$ = 0.917 V *vs.* RHE), which were better than those of Pt–Co@NC-800-10% (0.994 V, 0.889 V) and Pt–Zn@NC-800-10% (0.994 V, 0.886 V). E_{onset} and $E_{1/2}$ of Pt–CoZn@NC-800-10% positively shifted by 40 and 39 mV compared with commercial Pt/C (0.972 V, 0.878 V), respectively.

Fig. 4b compares the mass activities and specific activities of these catalysts calculated from the kinetic current density at 0.9 V *vs.* RHE. Accordingly, the ternary Pt–CoZn@NC-800-10% catalyst exhibited the optimal performances with a mass activity of 0.37 mA μg_{Pt}^{-1} and specific activity of 1.50 mA cm^{-2} (Table S2, ESI†). In addition, the Tafel plots (Fig. 4c) indicate the highest inherent catalytic kinetics of Pt–CoZn@NC-800-10% at any given potential because it had the smallest Tafel slope of 55 mV dec^{-1} among all the catalysts.[46] According to previous studies, the introduction of a third metal may boost ORR catalysis by decreasing the hydroxyl (OH) adsorption

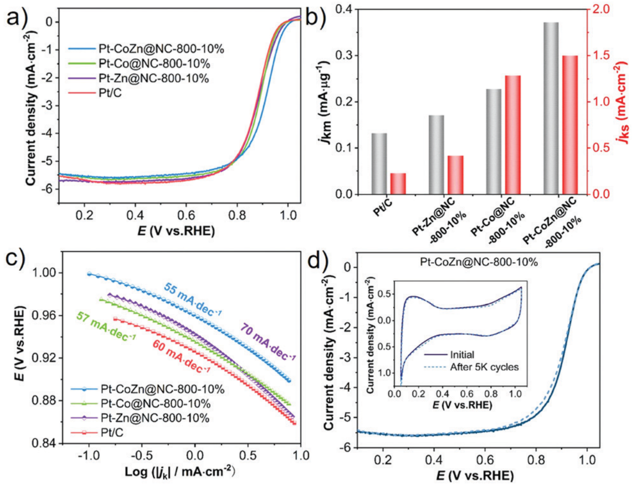

Fig. 4 ORR performance of the three products obtained at 800 °C with 10 wt_{Pt}% loading and commercial Pt/C. (a) Polarization curves in O_2-saturated 0.1 M $HClO_4$ at 1600 rpm with 85% iR compensation and a scan rate of 10 mV s^{-1}. (b) Comparisons of the mass activities and specific activities at 0.9 V *vs.* RHE. (c) Tafel plots for the ORR tests. (d) CV curves in N_2-saturated 0.1 M $HClO_4$ with a scan rate of 50 mV s^{-1} and polarization curves of the Pt–CoZn@NC-800-10% catalyst before and after 5000 cycles for ADT performance.

energy due to synergy between the compressive strain and ligand effects.[48–50]

Coincidently, the ternary Pt–CoZn@NC-800-10% catalyst also demonstrated long-term durability in the accelerated durability tests (ADTs) with a sweep rate of 100 mV s^{-1} between 0.6 and 1.0 V *vs.* RHE in O_2-saturated 0.1 M $HClO_4$. After 5000 sweep cycles, the CV curves still showed typical electrochemical characteristics of Pt-based catalysts without an obvious change. There was a slightly negative shift in $E_{1/2}$ (1 mV loss) according to the polarization curves (Fig. 4d). The same tests were conducted to assess the cycling stability of commercial Pt/C, Pt–Zn@NC-800-10%, and Pt-Co@NC-800-10% catalysts (Fig. S7a–c, ESI†), which indicated 9 mV, 17 mV, and 8 mV loss in $E_{1/2}$ after ADTs, respectively. Moreover, as shown in Fig. S7d (ESI†), the mass activity and ECSA of the Pt–CoZn@NC-800-10% catalyst decreased by 16.2% and 9%, respectively, greatly surpassing those of the other catalysts. TEM observations (Fig. S8, ESI†) revealed that after ADTs, the encapsulation structure of the NC layer on alloy NPs was well preserved, and the size and overall morphology of alloy particles remained unchanged. The high stability of alloy catalysts was attributed to the NC matrix pyrolyzed from ZIFs. The doping of N in the carbon matrix may alter the electronic properties of the alloy's nanostructure, resulting in enhanced interactions between the alloy NPs and supports.[51,52] In a word, the Pt–CoZn alloy wrapped with NC was superior to those binary alloy catalysts with similar structures and traditional Pt/C catalysts in its ORR mass activity and durability.

Affecting factors of Pt–CoZn@NC catalysts

To obtain the optimal catalyst, the effects of pyrolysis temperature and Pt loading on the performances of the pyrolysis-derived products (Pt–CoZn@NC-10%) were investigated. Firstly, the pyrolysis temperature greatly affected the carbonization and alloying processes of the catalysts. As shown in Fig. 5a, the Pt–CoZn@NC-700-10% was composed of a mixed PtZn intermetallic phase and fcc-structured PtCo alloy. On the other hand, the Pt–CoZn@NC-900-10% catalyst was almost composed only of a fcc-structured PtCo alloy because the Zn species would evaporate at 900 °C (bp: 907 °C). In contrast, the crystal structure of alloy metal NPs was completely transformed into the fcc-phase when the pyrolysis temperature reached 800 °C (*i.e.*, Pt–CoZn@NC-800-10%), which was considered as the ternary-alloy structure integrated with Pt–Co and a small amount of Zn. Raman spectra in Fig. 5b show the detailed carbon structure of Pt–CoZn@NC-10% catalysts. By comparing the peak intensity ratios (I_D/I_G) of the products, it can be found that there are abundant defects in the carbon layer, which may provide plentiful active sites for ORR electrocatalysis.

In addition, N species in the carbon matrix of Pt–CoZn@NC-10% were also analyzed by XPS (Fig. 5c). As revealed in Table S3 (ESI†), Pt–CoZn@NC-800-10% had the highest total proportion of pyridinic N and graphitic N in the NC shell (66.6%) and was therefore expected to achieve the best ORR catalytic performance.

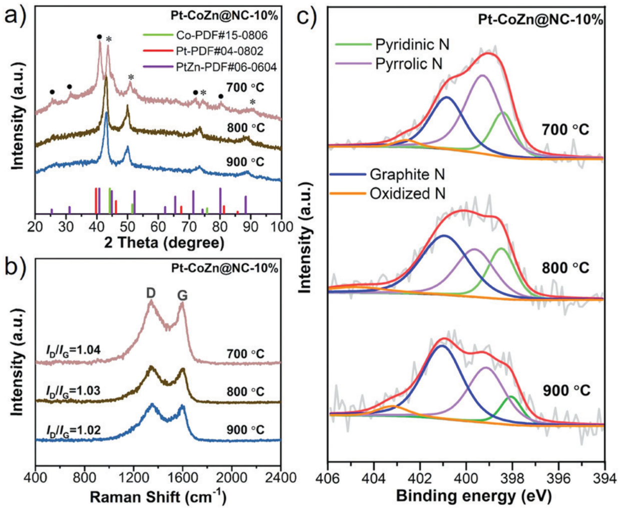

Fig. 5 (a) XRD patterns. * and ● denote the diffraction peaks for the fcc-structured PtCo alloy and intermetallic PtZn, respectively; (b) Raman spectra; (c) high-resolution N 1s XPS spectra of Pt–CoZn@NC-10% samples obtained at 700, 800 and 900 °C.

We also studied the effect of pyrolysis temperature on Pt–CoZn@NC-10% catalysts for the ORR. As shown in Fig. 6a, Pt–CoZn@NC-800-10% exhibited a superior catalytic performance, since the half-wave potential ($E_{1/2}$) of the polarization curve (0.917 V) was distinctly higher than those for Pt–CoZn@NC-700-10% (0.862 V) and Pt–CoZn@NC-900-10% (0.859 V). Both the mass activity and specific activity revealed a volcano-shaped trend (Fig. 6b) upon increasing the pyrolysis temperature. The above results indicate that insufficient or excessive pyrolysis deteriorated the electrocatalytic properties of the alloy catalysts. Combined with the above analyses of the alloy composition and NC shell, it can be determined that the Pt–CoZn@NC-800-10% catalyst possessed the most active sites for the ORR, probably due to its optimal alloy structure and NC matrix.

To evaluate the influence of Pt content on the activity of the catalysts in the ORR, we further fabricated a series of Pt@CoZn-ZIF precursors with different mass loadings of Pt NPs (1%, 5%, and 10%) and converted them into the desired products at the optimal pyrolysis temperature of 800 °C. CV curves (Fig. S9a, ESI†) showed that the product with 1 wt_{Pt}% did not display characteristics indicative of hydrogen desorption and oxide reduction, and the ORR polarization curve did not reach the

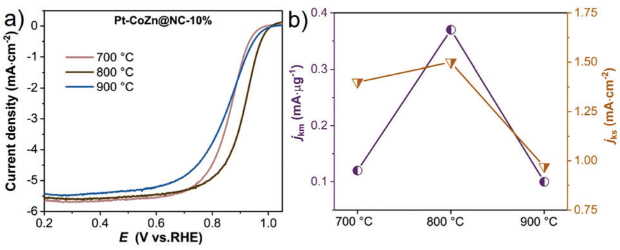

Fig. 6 (a) ORR polarization curves; (b) mass activity and specific activity for Pt–CoZn@NC-10% samples obtained at calcination temperatures of 700, 800, and 900 °C.

theoretical limiting diffusion current density (Fig. S9b, ESI†). This might be mainly due to the low Pt content of Pt–CoZn@NC-800-1% (only 1.1 wt%, Table S1, ESI†). Once the Pt loading was increased to 5 wt%, the ORR catalytic performance increased with an E_{onset} of 0.999 V and $E_{1/2}$ of 0.896 V (Table S4, ESI†), but it was still inferior to that of the samples with 10 $\text{wt}_{\text{Pt}}\%$ (E_{onset} of 1.012 V, $E_{1/2}$ of 0.917 V). Based on the above results, it can be concluded that the excellent electrocatalytic performances of Pt–CoZn@NC-800-10% are a result of many factors including the phase and exposing status of alloy NP as well as the N form and content of NC matrix.

Conclusions

Here, we demonstrated a facile protocol to synthesize a hybrid-structured ternary Pt–CoZn alloy encapsulated within N-doped carbon by the pyrolysis of Pt@CoZn-ZIF precursors. To determine the optimal synthetic conditions of the Pt-CoZn@NC catalyst, the pyrolysis temperature and Pt loading were systematically adjusted. In the acidic ORR, Pt–CoZn@NC-800-10% exhibited significantly enhanced catalytic activity with an $E_{1/2}$ reaching 0.917 V (*vs.* RHE). It also showed a much lower decrease in ECSA and $E_{1/2}$ after 5000 ADT cycles compared with both the commercial Pt/C catalyst and binary alloy hybrid catalysts (Pt-Co@NC-800-10% and Pt–Zn@NC-800-10%). The excellent performance of Pt–CoZn@NC-800-10% was mainly ascribed to the electronic interactions between Pt, Co, and Zn species, as well as the synergistic effect of N species in the carbon matrix. Overall, this study provides a promising design strategy for obtaining high-performance ORR electrocatalysts with improved activity and stability.

Conflicts of interest

There are no conflicts to declare.

Acknowledgements

This work was supported by the National Key R&D Program of China (2020YFB1505800) and the National Natural Science Foundation of China (No. 22071202, 21931009, 21721001, and 21773190).

References

1 W. Tu, W. Luo, C. Chen, K. Chen, E. Zhu, Z. Zhao, Z. Wang, T. Hu, H. Zai, X. Ke, M. Sui, P. Chen, Q. Zhang, Q. Chen, Y. Li and Y. Huang, Tungsten as "adhesive" in $Pt_2CuW_{0.25}$ ternary alloy for highly durable oxygen reduction electrocatalysis, *Adv. Funct. Mater.*, 2019, **30**, 1908230.

2 Y. Nie, L. Li and Z. Wei, Recent advancements in Pt and Pt-free catalysts for oxygen reduction reaction, *Chem. Soc. Rev.*, 2015, **44**, 2168–2201.

3 L. Zhang, K. Doyle-Davis and X. Sun, Pt-Based electrocatalysts with high atom utilization efficiency: from nanostructures to single atoms, *Energy Environ. Sci.*, 2019, **12**, 492–517.

4 L. Du, L. Xing, G. Zhang and S. Sun, Metal-organic framework derived carbon materials for electrocatalytic oxygen reactions: Recent progress and future perspectives, *Carbon*, 2020, **156**, 77–92.

5 W. Xia, J. Zhu, W. Guo, L. An, D. Xia and R. Zou, Well-defined carbon polyhedrons prepared from nano metal–organic frameworks for oxygen reduction, *J. Mater. Chem. A*, 2014, **2**, 11606–11613.

6 Z. Wang, H. Jin, T. Meng, K. Liao, W. Meng, J. Yang, D. He, Y. Xiong and S. Mu, Fe, Cu-coordinated ZIF-derived carbon framework for efficient oxygen reduction reaction and zinc-air batteries, *Adv. Funct. Mater.*, 2018, **28**, 1802596.

7 M. Shen, M. Xie, J. Slack, K. Waldrop, Z. Chen, Z. Lyu, S. Cao, M. Zhao, M. Chi, P. N. Pintauro, R. Cao and Y. Xia, Pt-Co truncated octahedral nanocrystals: a class of highly active and durable catalysts toward oxygen reduction, *Nanoscale*, 2020, **12**, 11718–11727.

8 D. Y. Chung, S. W. Jun, G. Yoon, S. G. Kwon, D. Y. Shin, P. Seo, J. M. Yoo, H. Shin, Y. H. Chung, H. Kim, B. S. Mun, K. S. Lee, N. S. Lee, S. J. Yoo, D. H. Lim, K. Kang, Y. E. Sung and T. Hyeon, Highly durable and active PtFe nanocatalyst for electrochemical oxygen reduction reaction, *J. Am. Chem. Soc.*, 2015, **137**, 15478–15485.

9 M. Oezaslan and P. Strasser, Activity of dealloyed $PtCo_3$ and $PtCu_3$ nanoparticle electrocatalyst for oxygen reduction reaction in polymer electrolyte membrane fuel cell, *J. Power Sources*, 2011, **196**, 5240–5249.

10 X. Q. Huang, Z. P. Zhao, L. Cao, Y. Chen, E. B. Zhu, Z. Y. Lin, M. F. Li, A. M. Yan, A. Zettl, Y. M. Wang, X. F. Duan, T. Mueller and Y. Huang, High-performance transition metal-doped Pt_3Ni octahedra for oxygen reduction reaction, *Science*, 2015, **348**, 1230–1234.

11 Z. Qi, Y. Pei, T. W. Goh, Z. Wang, X. Li, M. Lowe, R. V. Maligal-Ganesh and W. Huang, Conversion of confined metal@ZIF-8 structures to intermetallic nanoparticles supported on nitrogen-doped carbon for electrocatalysis, *Nano Res.*, 2018, **11**, 3469–3479.

12 Z. Zhu, Y. Zhai and S. Dong, Facial synthesis of PtM (M = Fe, Co, Cu, Ni) bimetallic alloy nanosponges and their enhanced catalysis for oxygen reduction reaction, *ACS Appl. Mater. Interfaces*, 2014, **6**, 16721–16726.

13 J. Lai, F. Lin, Y. Tang, P. Zhou, Y. Chao, Y. Zhang and S. Guo, Efficient bifunctional polyalcohol oxidation and oxygen reduction electrocatalysts enabled by ultrathin PtPdM (M = Ni, Fe, Co) nanosheets, *Adv. Energy Mater.*, 2019, **9**, 1800684.

14 Y. J. Wang, N. Zhao, B. Fang, H. Li, X. T. Bi and H. Wang, Carbon-supported Pt-based alloy electrocatalysts for the oxygen reduction reaction in polymer electrolyte membrane fuel cells: particle size, shape, and composition manipulation and their impact to activity, *Chem. Rev.*, 2015, **115**, 3433–3467.

15 D. Wang, H. L. Xin, R. Hovden, H. Wang, Y. Yu, D. A. Muller, F. J. DiSalvo and H. D. Abruna, Structurally ordered

intermetallic platinum-cobalt core-shell nanoparticles with enhanced activity and stability as oxygen reduction electrocatalysts, *Nat. Mater.*, 2013, **12**, 81–87.

16 X. Tan, S. Prabhudev, A. Kohandehghan, D. Karpuzov, G. A. Botton and D. Mitlin, Pt–Au–Co alloy electrocatalysts demonstrating enhanced activity and durability toward the oxygen reduction reaction, *ACS Catal.*, 2015, **5**, 1513–1524.

17 Q. Chen, Z. Cao, G. Du, Q. Kuang, J. Huang, Z. Xie and L. Zheng, Excavated octahedral Pt-Co alloy nanocrystals built with ultrathin nanosheets as superior multifunctional electrocatalysts for energy conversion applications, *Nano Energy*, 2017, **39**, 582–589.

18 M. Lokanathan, I. M. Patil, P. Mukherjee, A. Swami and B. Kakade, Molten-Salt synthesis of Pt_3Co binary alloy nanoplates as excellent and durable electrocatalysts toward oxygen electroreduction, *ACS Sustainable Chem. Eng.*, 2019, **8**, 986–993.

19 J. Liang, Z. Zhao, N. Li, X. Wang, S. Li, X. Liu, T. Wang, G. Lu, D. Wang, B. J. Hwang, Y. Huang, D. Su and Q. Li, Biaxial strains mediated oxygen reduction electrocatalysis on Fenton reaction resistant $L1_0$-PtZn fuel cell cathode, *Adv. Energy Mater.*, 2020, **10**, 2000179.

20 Y. Wu, Y. Zhao, J. Liu and F. Wang, Adding refractory 5d transition metal W into PtCo system: an advanced ternary alloy for efficient oxygen reduction reaction, *J. Mater. Chem. A*, 2018, **6**, 10700–10709.

21 M. T. Liu, L. X. Chen, A. J. Wang, K. M. Fang and J. J. Feng, Ternary PtCoNi flower-like networks: One-step additive-free synthesis and highly boosted electrocatalytic performance for hydrogen evolution and oxygen reduction, *Int. J. Hydrogen Energy*, 2017, **42**, 25277–25284.

22 X. Zhong, W. Xu, L. Wang, Y. Qin, G. Zhuang, X. Li and J. G. Wang, Twin-like ternary PtCoFe alloy in nitrogen-doped graphene nanopores as a highly effective electrocatalyst for oxygen reduction, *Catal. Sci. Technol.*, 2016, **6**, 5942–5948.

23 M. Ishida and K. Matsutani, Development of high durability PtCoMn catalyst for PEFCs, *ECS Trans.*, 2017, **80**, 725–729.

24 A. Oh, Y. J. Sa, H. Hwang, H. Baik, J. Kim, B. Kim, S. H. Joo and K. Lee, Rational design of Pt-Ni-Co ternary alloy nanoframe crystals as highly efficient catalysts toward the alkaline hydrogen evolution reaction, *Nanoscale*, 2016, **8**, 16379–16386.

25 K. A. Kuttiyiel, K. Sasaki, Y. Choi, D. Su, P. Liu and R. R. Adzic, Nitride stabilized PtNi core-shell nanocatalyst for high oxygen reduction activity, *Nano Lett.*, 2012, **12**, 6266–6271.

26 S. Liu, Z. Wang, S. Zhou, F. Yu, M. Yu, C. Y. Chiang, W. Zhou, J. Zhao and J. Qiu, Metal-Organic-Framework-Derived hybrid carbon nanocages as a bifunctional electrocatalyst for oxygen reduction and evolution, *Adv. Mater.*, 2017, **29**, 1700874.

27 J. Wang, G. Han, L. Wang, L. Du, G. Chen, Y. Gao, Y. Ma, C. Du, X. Cheng, P. Zuo and G. Yin, ZIF-8 with ferrocene encapsulated: a promising precursor to single-atom Fe embedded nitrogen-doped carbon as highly efficient catalyst for oxygen electroreduction, *Small*, 2018, **14**, e1704282.

28 W. Yang, X. Li, Y. Li, R. Zhu and H. Pang, Applications of Metal-Organic-Framework-Derived carbon materials, *Adv. Mater.*, 2019, **31**, e1804740.

29 X. Ao, W. Zhang, B. Zhao, Y. Ding, G. Nam, L. Soule, A. A. Abdelhafiz, C. Wang and M. Liu, Atomically dispersed Fe-N-C decorated with Pt-alloy core-shell nanoparticles for improved activity and durability towards oxygen reduction, *Energy Environ. Sci.*, 2020, **13**, 3032–3040.

30 A. Phan, C. J. Doonan, F. J. Uribe-Romo, C. B. Knobler, M. O'Keeffe and O. M. Yaghi, Synthesis, structure, and carbon dioxide capture properties of zeolitic imidazolate frameworks, *Acc. Chem. Res.*, 2010, **43**, 58–67.

31 Y. Z. Chen, C. Wang, Z. Y. Wu, Y. Xiong, Q. Xu, S. H. Yu and H. L. Jiang, From bimetallic Metal-Organic Framework to porous carbon: high surface area and multicomponent active dopants for excellent electrocatalysis, *Adv. Mater.*, 2015, **27**, 5010–5016.

32 X. Lou, Y. Ning, C. Li, X. Hu, M. Shen and B. Hu, Bimetallic zeolite imidazolate framework for enhanced lithium storage boosted by the redox participation of nitrogen atoms, *Sci. China Mater.*, 2018, **61**, 1040–1048.

33 Z. Lu, B. Wang, Y. Hu, W. Liu, Y. Zhao, R. Yang, Z. Li, J. Luo, B. Chi, Z. Jiang, M. Li, S. Mu, S. Liao, J. Zhang and X. Sun, An isolated Zinc-Cobalt atomic pair for highly active and durable oxygen reduction, *Angew. Chem., Int. Ed.*, 2019, **58**, 2622–2626.

34 L. Liang, H. Jin, H. Zhou, B. Liu, C. Hu, D. Chen, Z. Wang, Z. Hu, Y. Zhao, H.-W. Li, D. He and S. Mu, Cobalt single atom site isolated Pt nanoparticles for efficient ORR and HER in acid media, *Nano Energy*, 2021, **88**, 106221.

35 L. Liang, H. jin, H. Zhou, B. Liu, C. Hu, D. Chen, J. Zhu, Z. Wang, H.-W. Li, S. Liu, D. He and S. Mu, Ultra-small platinum nanoparticles segregated by nickle sites for efficient ORR and HER processes, *J. Energy Chem.*, 2022, **65**, 48–54.

36 Y. Xue, H. Li, X. Ye, S. Yang, Z. Zheng, X. Han, X. Zhang, L. Chen, Z. Xie, Q. Kuang and L. Zheng, N-doped carbon shell encapsulated PtZn intermetallic nanoparticles as highly efficient catalysts for fuel cells, *Nano Res.*, 2019, **12**, 2490–2497.

37 G. Lu, S. Li, Z. Guo, O. K. Farha, B. G. Hauser, X. Qi, Y. Wang, X. Wang, S. Han, X. Liu, J. S. DuChene, H. Zhang, Q. Zhang, X. Chen, J. Ma, S. C. Loo, W. D. Wei, Y. Yang, J. T. Hupp and F. Huo, Imparting functionality to a metal-organic framework material by controlled nanoparticle encapsulation, *Nat. Chem.*, 2012, **4**, 310–316.

38 X. Han, Z. Zheng, J. Chen, Y. Xue, H. Li, J. Zheng, Z. Xie, Q. Kuang and L. Zheng, Efficient oxygen reduction on sandwich-like metal@N-C composites with ultrafine Fe nanoparticles embedded in N-doped carbon nanotubes grafted on graphene sheets, *Nanoscale*, 2019, **11**, 12610–12618.

39 Z. Hu, Z. Zhang, Z. Li, M. Dou and F. Wang, One-Step conversion from core-shell Metal-Organic Framework

materials to cobalt and nitrogen codoped carbon nanopolyhedra with hierarchically porous structure for highly efficient oxygen reduction, *ACS Appl. Mater. Interfaces*, 2017, **9**, 16109–16116.

40 B. You, N. Jiang, M. Sheng, W. S. Drisdell, J. Yano and Y. Sun, Bimetal–Organic Framework self-adjusted synthesis of support-free nonprecious electrocatalysts for efficient oxygen reduction, *ACS Catal.*, 2015, **5**, 7068–7076.

41 W. Zhang, G. Lu, C. Cui, Y. Liu, S. Li, W. Yan, C. Xing, Y. R. Chi, Y. Yang and F. Huo, A family of metal-organic frameworks exhibiting size-selective catalysis with encapsulated noble-metal nanoparticles, *Adv. Mater.*, 2014, **26**, 4056–4060.

42 S. Ratso, I. Kruusenberg, M. Vikkisk, U. Joost, E. Shulga, I. Kink, T. Kallio and K. Tammeveski, Highly active nitrogen-doped few-layer graphene/carbon nanotube composite electrocatalyst for oxygen reduction reaction in alkaline media, *Carbon*, 2014, **73**, 361–370.

43 Q. Wang, Q. Zhao, Y. Su, G. Zhang, G. Xu, Y. Li, B. Liu, D. Zheng and J. Zhang, Hierarchical carbon and nitrogen adsorbed PtNiCo nanocomposites with multiple active sites for oxygen reduction and methanol oxidation reactions, *J. Mater. Chem. A*, 2016, **4**, 12296–12307.

44 Q. Wang, S. Chen, H. Lan, P. Li, X. Ping, S. Ibraheem, D. Long, Y. Duan and Z. Wei, Thermally driven interfacial diffusion synthesis of nitrogen-doped carbon confined trimetallic Pt_3CoRu composites for the methanol oxidation reaction, *J. Mater. Chem. A*, 2019, **7**, 18143–18149.

45 C. Li, Q. Yuan, B. Ni, T. He, S. Zhang, Y. Long, L. Gu and X. Wang, Dendritic defect-rich palladium-copper-cobalt nanoalloys as robust multifunctional non-platinum electrocatalysts for fuel cells, *Nat. Commun.*, 2018, **9**, 3702.

46 G. M. Leteba, D. R. G. Mitchell, P. B. J. Levecque and C. I. Lang, Solution-grown dendritic Pt-based ternary nanostructures for enhanced oxygen reduction reaction functionality, *Nanomaterials*, 2018, **8**, 462.

47 T. Wang, J. Liang, Z. Zhao, S. Li, G. Lu, Z. Xia, C. Wang, J. Luo, J. Han, C. Ma, Y. Huang and Q. Li, Sub-6 nm fully ordered $L1_0$-Pt–Ni–Co nanoparticles enhance oxygen reduction via Co doping induced ferromagnetism enhancement and optimized surface strain, *Adv. Energy Mater.*, 2019, **9**, 1803771.

48 W. Zhang, J. Zhu, D. Cheng and X. C. Zeng, PtCoNi alloy nanoclusters for synergistic catalytic oxygen reduction reaction, *ACS Appl. Nano Mater.*, 2020, **3**, 2536–2544.

49 A. Kulkarni, S. Siahrostami, A. Patel and J. K. Norskov, Understanding catalytic activity trends in the oxygen reduction reaction, *Chem. Rev.*, 2018, **118**, 2302–2312.

50 K. Li, X. Li, H. Huang, L. Luo, X. Li, X. Yan, C. Ma, R. Si, J. Yang and J. Zeng, One-Nanometer-Thick PtNiRh trimetallic nanowires with enhanced oxygen reduction electrocatalysis in acid media: integrating multiple advantages into one catalyst, *J. Am. Chem. Soc.*, 2018, **140**, 16159–16167.

51 P. Yin, T. Yao, Y. Wu, L. Zheng, Y. Lin, W. Liu, H. Ju, J. Zhu, X. Hong, Z. Deng, G. Zhou, S. Wei and Y. Li, Single cobalt atoms with precise N-coordination as superior oxygen reduction reaction catalysts, *Angew. Chem., Int. Ed.*, 2016, **55**, 10800–10805.

52 X. X. Wang, S. Hwang, Y. T. Pan, K. Chen, Y. He, S. Karakalos, H. Zhang, J. S. Spendelow, D. Su and G. Wu, Ordered Pt_3Co intermetallic nanoparticles derived from Metal-Organic Frameworks for oxygen reduction, *Nano Lett.*, 2018, **18**, 4163–4171.